

Banner appropriate to article type will appear here in typeset article

A revised gap-averaged Floquet analysis of Faraday waves in Hele-Shaw cells

Alessandro Bongarzone^{1†}, Baptiste Jouron, Francesco Viola² and François Gallaire¹

¹Laboratory of Fluid Mechanics and Instabilities, École Polytechnique Fédérale de Lausanne, Lausanne, CH-1015, Switzerland

²Gran Sasso Science Institute, Viale F. Crispi, 7, 67100 L'Aquila, Italy

(Received xx; revised xx; accepted xx)

Existing theoretical analyses of Faraday waves in Hele-Shaw cells rely on the Darcy approximation and assume a parabolic flow profile in the narrow direction. However, Darcy's model is known to be inaccurate when convective or unsteady inertial effects are important. In this work, we propose a gap-averaged Floquet theory accounting for inertial effects induced by the unsteady terms in the Navier-Stokes equations, a scenario that corresponds to a pulsatile flow where the fluid motion reduces to a two-dimensional oscillating Poiseuille flow, similarly to the Womersley flow in arteries. When gap-averaging the linearized Navier-Stokes equation, this results in a modified damping coefficient, which is a function of the ratio between the Stokes boundary layer thickness and the cell's gap, and whose complex value depends on the frequency of the wave response specific to each unstable parametric region. We first revisit the standard case of horizontally infinite rectangular Hele-Shaw cells by also accounting for a dynamic contact angle model. A comparison with existing experiments shows the predictive improvement brought by the present theory and points out how the standard gap-averaged model often underestimates the Faraday threshold. The analysis is then extended to the less conventional case of thin annuli. A series of dedicated experiments for this configuration highlights how Darcy's thin-gap approximation overlooks a frequency detuning that is essential to correctly predict the locations of the Faraday tongues in the frequency-amplitude parameter plane. These findings are well rationalized and captured by the present model.

1. Introduction

Recent Hele-Shaw cell experiments have enriched the knowledge of Faraday waves (Faraday 1831). Researchers have uncovered a new type of highly localized standing waves, referred to as oscillons, that are both steep and solitary-like in nature (Rajchenbach *et al.* 2011). These findings have spurred further experimentations with Hele-Shaw cells filled with one or more liquid layers, using a variety of fluids, ranging from silicone oil, and water-ethanol mixtures to pure ethanol (Li *et al.* 2018*b*). Through these experiments, new combined patterns produced by triadic interactions of oscillons were discovered by Li *et al.* (2014). Additionally, another new family of waves was observed in a cell filled solely with pure ethanol and at extremely

† Email address for correspondence: alessandro.bongarzone@epfl.ch

shallow liquid depths (Li *et al.* 2015, 2016).

All these findings contribute to the understanding of the wave behaviour in Hele-Shaw configurations and call for a reliable stability theory that can explain and predict the instability onset for the emergence of initial wave patterns.

Notwithstanding two-dimensional direct numerical simulations (Périnet *et al.* 2016; Ubal *et al.* 2003) have been able to qualitatively replicate standing wave patterns reminiscent of those observed in experiments (Li *et al.* 2014), these simulations overlook the impact of wall attenuation, hence resulting in a simplified model that cannot accurately predict the instability regions (Benjamin & Ursell 1954; Kumar & Tuckerman 1994) and is therefore not suitable for modelling Hele-Shaw flows. On the other hand, attempting to conduct three-dimensional simulations of fluid motions in a Hele-Shaw cell poses a major challenge due to the high computational cost associated with the narrow dimension of the cell, which requires a smaller grid cell size to capture the shear dissipation accurately. Consequently, the cost of performing such simulations increases rapidly.

In order to tackle the challenges associated with resolving fluid dynamics within such systems, researchers have utilized Darcy’s law as an approach to treating the confined fluid between two vertical walls. This approximation, also used in the context of porous medium, considers the fluid to be flowing through a porous medium, resulting in a steady parabolic flow in the short dimension. When gap-averaging the linearized Navier-Stokes equation, this approximation translates into a damping coefficient σ that scales as $12\nu/b^2$, with ν the fluid kinematic viscosity and b the cell’s gap-size, which represents the boundary layer dissipation at the lateral walls. However, Darcy’s model is known to be inaccurate when convective and unsteady inertial effects are not negligible, such as in waves (Kalogirou *et al.* 2016). It is challenging to reintroduce convective terms consistently into the gap-averaged Hele-Shaw equations from a mathematical standpoint (Ruyer-Quil 2001; Plouraboué & Hinch 2002; Luchini & Charru 2010).

In their research, Li *et al.* (2019) applied the Kelvin-Helmholtz-Darcy theory proposed by Gondret & Rabaud (1997) to reintroduce advection and derive the nonlinear gap-averaged Navier-Stokes equations. These equations were then implemented in the open-source code *Gerris* developed by (Popinet 2003, 2009) to simulate Faraday waves in a Hele-Shaw cell. Although this gap-averaged model was compared to several experiments and demonstrated fairly good agreement, it should be noted that the surface tension term remains two-dimensional, as the out-of-plane interface shape is not directly taken into account. This simplified treatment neglects the contact line dynamics and may lead to miscalculations in certain situations. Advances in this direction were made by Li *et al.* (2018a), who found that the out-of-plane capillary forces associated with the meniscus curvature across the thin-gap direction should be retained in order to improve the description of the wave dynamics, as experimental evidence suggests. By employing a more sophisticated model, coming from molecular kinetics theory (Blake 1993; Hamraoui *et al.* 2000; Blake 2006) and similar to the macroscopic one introduced by Hocking (1987), to include the capillary contact line motion arising from the small scale of the gap-size between the two walls of a Hele-Shaw cell, they derived a novel dispersion relation, which indeed better predicts the observed instability onset.

However, discrepancies in the instability thresholds were still found. This mismatch was tentatively attributed to factors that are not accounted for in the gap-averaged model, such as the extra dissipation on the lateral walls in the elongated direction. Of course, a lab-scale experiment using a rectangular cell cannot entirely replace an infinite-length model, but if the container is sufficiently long, then this extra dissipation should be negligible. Other candidates were identified in the phenomenological contact line model or free surface contaminations.

If these factors can certainly be sources of discrepancies, we believe that a pure hydrody-

dynamic effect could be at the origin of the discordance between theory and experiments in the first place.

Despite the use of the Darcy approximation is well-assessed in the literature, the choice of a steady Poiseuille flow profile as an ansatz to build the gap-averaged model appears in fundamental contrast with the unsteady nature of oscillatory Hele-Shaw flows, such as Faraday waves. At low enough oscillation frequencies or for sufficiently viscous fluids, the thickness of the oscillating Stokes boundary layer becomes comparable to the cell gap: the Stokes layers over the lateral solid faces of the cell merge and eventually invade the entire fluid bulk. In such scenarios, the Poiseuille profile gives an adequate flow description, but this pre-requisite is rarely met in the above-cited experimental campaigns. It appears, thus, very natural to ask oneself whether a more appropriate description of the oscillating boundary layer impacts the prediction of stability boundaries. This study is precisely devoted to answering this question by proposing a revised gap-averaged Floquet analysis, based on the classical Womersley-like solution for the pulsating flow in a channel (Womersley 1955; San & Staples 2012).

Following the approach taken by Viola *et al.* (2017), we examine the impact of inertial effects on the instability threshold of Faraday waves in Hele-Shaw cells, with a focus on the unsteady term of the Navier-Stokes equations. This scenario corresponds to a pulsatile flow where the fluid's motion reduces to a two-dimensional oscillating channel flow, which seems better suited than the steady Poiseuille profile to investigate the stability properties of the system. When gap-averaging the linearized Navier-Stokes equation, this results in a modified damping coefficient becoming a function of the ratio between the Stokes boundary layer thickness and the cell's gap, and whose complex value will depend on the frequency of the wave response specific to each unstable parametric region.

First, we consider the case of horizontally infinite rectangular Hele-Shaw cells by also accounting for the same dynamic contact angle model employed by Li *et al.* (2019), so as to quantify the predictive improvement brought by the present theory. A *vis-à-vis* comparison with experiments by Li *et al.* (2019) points out how the standard Darcy model often underestimates the Faraday threshold, whereas the present theory can explain and close the gap with these experiments.

The analysis is then extended to the case of thin annuli. This less common configuration has been already used to investigate oscillatory phase modulation of parametrically forced surface waves (Douady *et al.* 1989) and drift instability of cellular patterns (Fauve *et al.* 1991). For our interest, an annular cell is convenient as it naturally filters out the extra dissipation that could take place on the lateral boundary layer in the elongated direction, hence allowing us to reduce the sources of extra uncontrolled dissipation and perform a cleaner comparison with experiments. Our homemade experiments for this configuration highlight how Darcy's theory overlooks a frequency detuning that is essential to correctly predict the locations of the Faraday's tongues in the frequency spectrum. These findings are well rationalized and captured by the present model.

The paper is organized as follows. In §2 we revisit the classical case of horizontally infinite rectangular Hele-Shaw cells. The present model is compared with theoretical predictions from the standard Darcy theory and with existing experiments. The case of thin annuli is then considered. The model for the latter unusual configuration is formulated in §3 and compared with homemade experiments in §4. Conclusions are outlined in §5.

2. Horizontally infinite Hele-Shaw cells

Let us begin by considering the case of a horizontally infinite Hele-Shaw cell of width b filled to a depth h with an incompressible fluid of density ρ , dynamic viscosity μ (kinematic

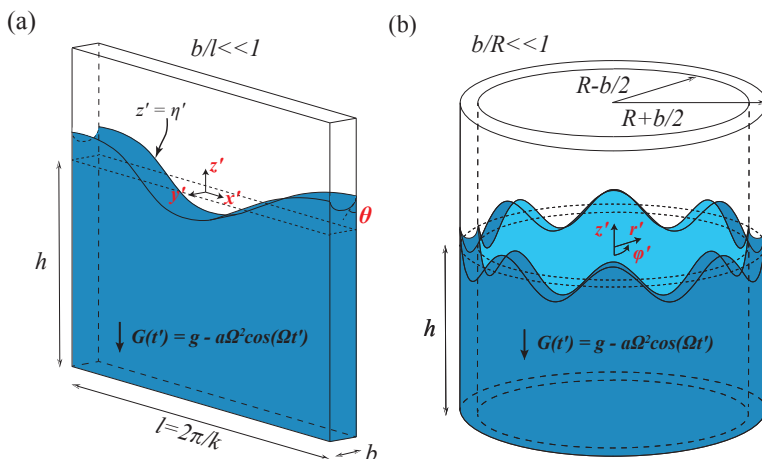


Figure 1: (a) Sketch of Faraday waves in a rectangular Hele-Shaw cell of width b and length l filled to a depth h with a liquid. Here b denotes the gap size of the Hele-Shaw cell, l is the wavelength of a certain wave, such that $b/l \ll 1$, and θ is the dynamic contact angle of the liquid on the lateral walls. The vessel undergoes a vertical sinusoidal oscillation of amplitude a and angular frequency Ω . The free surface elevation is denoted by $\eta'(x')$. (b) Same as (a), but in an annular Hele-Shaw cell with internal and external radii, respectively, $R - b/2$ and $R + b/2$. Here, $b/R \ll 1$ and the free surface elevation is a function of the azimuthal coordinate φ' , i.e. $\eta'(\varphi')$.

viscosity $\nu = \mu/\rho$) and liquid-air surface tension γ (see also sketch in figure 1(a)). The vessel undergoes a vertical sinusoidal oscillation of amplitude a and angular frequency Ω . In a frame of reference which moves with the oscillating container, the free liquid interface is flat and stationary for small forcing amplitudes, and the oscillation is equivalent to a temporally modulated gravitational acceleration, $G(t') = g - a\Omega^2 \cos \Omega t'$. The equation of motion for the fluid bulk are

$$\rho \left(\frac{\partial \mathbf{U}'}{\partial t'} + \mathbf{U}' \cdot \nabla' \mathbf{U}' \right) = -\nabla' P' + \mu \nabla'^2 \mathbf{U}' - \rho G(t') \mathbf{e}_z, \quad \nabla' \cdot \mathbf{U}' = 0. \quad (2.1)$$

Linearizing about the rest state $\mathbf{U}' = \mathbf{0}$ and $P'(z', t') = -\rho G(t') z'$, the equations for the perturbation velocity, $\mathbf{u}'(x', y', z', t') = \{u', v', w'\}^T$, and pressure, $p'(x', y', z', t')$, fields, associated with a certain perturbation's wavelength $l \sim k^{-1}$ (k , wavenumber), read

$$\rho \frac{\partial \mathbf{u}'}{\partial t'} = -\nabla' p' + \mu \nabla'^2 \mathbf{u}', \quad \nabla' \cdot \mathbf{u}' = 0. \quad (2.2)$$

Assuming that $bk \ll 1$, then the velocity along the narrow y' -dimension $v' \ll u', w'$ and, by employing the Hele-Shaw approximation as in, for instance, Viola *et al.* (2017), one can simplify the linearized Navier-Stokes equations as follows:

$$\frac{\partial u'}{\partial x'} + \frac{\partial v'}{\partial y'} + \frac{\partial w'}{\partial z'} = 0, \quad (2.3a)$$

$$\rho \frac{\partial u'}{\partial t'} = -\frac{\partial p'}{\partial x'} + \mu \frac{\partial^2 u'}{\partial y'^2}, \quad \rho \frac{\partial w'}{\partial t'} = -\frac{\partial p'}{\partial z'} + \mu \frac{\partial^2 w'}{\partial y'^2}, \quad \frac{\partial p'}{\partial y'} = 0. \quad (2.3b)$$

Equations (2.3a)-(2.3b) are made dimensionless using k^{-1} for the directions x and z , and b for y . The forcing amplitude and frequency provide a scale $a\Omega$ for the in-plane xz -velocity components, whereas the continuity equation imposes the transverse component v' to scale as $bka\Omega \ll a\Omega$, due to the strong confinement in the y -direction ($bk \ll 1$). With these choices, dimensionless spatial scales, velocity components and pressure write:

$$x = x'k, \quad y = \frac{y'}{b}, \quad z = z'k, \quad u = \frac{u'}{a\Omega^2}, \quad v = \frac{v'}{bka\Omega}, \quad w = \frac{w'}{a\Omega}, \quad p = \frac{kp'}{\rho a\Omega^2}. \quad (2.4)$$

The first two equations in (2.3b) in a non-dimensional form are

$$\frac{\partial u}{\partial t} = -\frac{\partial p}{\partial x} + \frac{\delta_{St}^2}{2} \frac{\partial^2 u}{\partial y^2}, \quad \frac{\partial w}{\partial t} = -\frac{\partial p}{\partial z} + \frac{\delta_{St}^2}{2} \frac{\partial^2 w}{\partial y^2}, \quad (2.5)$$

where $\delta_{St} = \delta'_{St}/b$ and with $\delta'_{St} = \sqrt{2\nu/\Omega}$ denoting the thickness of the oscillating Stokes boundary layer. The ratio $\sqrt{2}/\delta_{St}$ is also commonly referred to as the Womersley number, $Wo = b\sqrt{\Omega/\nu}$ (Womersley 1955; San & Staples 2012).

2.1. Floquet analysis of the gap-averaged equations

Given its periodic nature, the stability of the base flow, represented by a time-periodic modulation of the hydrostatic pressure, can be investigated via Floquet analysis. We therefore introduce the following Floquet ansatz (Kumar & Tuckerman 1994)

$$\mathbf{u}(x, y, z, t) = e^{\mu_F t} \sum_{n=-\infty}^{+\infty} \tilde{\mathbf{u}}_n(x, y, z) e^{i(n+\alpha/\Omega)t} = e^{\mu_F t} \sum_{n=-\infty}^{+\infty} \tilde{\mathbf{u}}_n(x, y, z) e^{i\xi_n t}, \quad (2.6a)$$

$$p(x, z, t) = e^{\mu_F t} \sum_{n=-\infty}^{+\infty} \tilde{p}_n(x, z) e^{i(n+\alpha/\Omega)t} = e^{\mu_F t} \sum_{n=-\infty}^{+\infty} \tilde{p}_n(x, z) e^{i\xi_n t}, \quad (2.6b)$$

where μ_F is the real part of the non-dimensional Floquet exponent and represents the growth rate of the perturbation. We have rewritten $(n + \alpha/\Omega) = \xi$ to better explicit the parametric nature of the oscillation frequency of the wave response. In the following, we will focus on the condition for marginal stability (boundaries of the Faraday's tongues), which require the growth rate $\mu_F = 0$. In addition, values of $\alpha = 0$ and $\Omega/2$ correspond, respectively, to harmonic and sub-harmonic parametric resonances (Kumar & Tuckerman 1994). This implies that ξ is a parameter whose value is either n , for harmonics, or $n + 1/2$, for sub-harmonics, with n an integer $n = 0, 1, 2, \dots$. We will therefore use only a discrete version of ξ , namely ξ_n , with the index n specific to each Fourier component in (2.6a)-(2.6b).

By injecting the ansatz (2.6a)-(2.6b) in (2.5), we find that each component of the Fourier series must satisfy

$$\forall n: \quad i\xi_n \tilde{u}_n = -\frac{\partial \tilde{p}_n}{\partial x} + \frac{\delta_{St}^2}{2} \frac{\partial^2 \tilde{u}_n}{\partial y^2}, \quad i\xi_n \tilde{w}_n = -\frac{\partial \tilde{p}_n}{\partial z} + \frac{\delta_{St}^2}{2} \frac{\partial^2 \tilde{w}_n}{\partial y^2}, \quad (2.7)$$

which, along with the no-slip condition at $y = \pm 1/2$, correspond to a two-dimensional pulsatile Poiseuille flow with solution

$$\tilde{u}_n = \frac{i}{\xi_n} \frac{\partial \tilde{p}_n}{\partial x} F_n(y), \quad \tilde{w}_n = \frac{i}{\xi_n} \frac{\partial \tilde{p}_n}{\partial z} F_n(y), \quad F_n(y) = \left(1 - \frac{\cosh(1+i)y/\delta_n}{\cosh(1+i)/2\delta_n}\right), \quad (2.8)$$

and where $\delta_n = \delta_{St}/\sqrt{\xi_n}$, is a rescaled Stokes boundary layer thickness specific to the n th Fourier component. The function $F_n(y)$ is displayed in figure 2(b), which depicts how a

decrease in the value of δ_n starting from large values corresponds to a progressive transition from a fully developed flow profile to a plug flow connected to thin boundary layers.

The gap-averaged velocity along the y -direction satisfies a Darcy-like equation,

$$\langle \tilde{\mathbf{u}}_n \rangle = \int_{-1/2}^{1/2} \tilde{\mathbf{u}}_n dy = \frac{i\beta_n}{\xi_n} \nabla \tilde{p}_n, \quad \beta_n = 1 - \frac{2\delta_n}{1+i} \tanh \frac{1+i}{2\delta_n}. \quad (2.9)$$

In order to obtain a governing equation for the pressure \tilde{p}_n , we average the continuity equation and we impose the impermeability condition for the span-wise velocity, $v = 0$ at $y = \pm 1/2$,

$$\frac{\partial \langle \tilde{u}_n \rangle}{\partial x} + \underbrace{\int_{-1/2}^{1/2} \frac{\partial \tilde{v}_n}{\partial y} dy}_{v(1/2) - v(-1/2) = 0} + \frac{\partial \langle \tilde{w}_n \rangle}{\partial z} = \nabla \cdot \langle \tilde{\mathbf{u}}_n \rangle = 0, \quad (2.10)$$

Since $\langle \tilde{\mathbf{u}}_n \rangle = i(\beta_n/\xi_n) \nabla \tilde{p}_n$, the pressure field \tilde{p}_n must obey the Laplace equation

$$\nabla^2 \tilde{p}_n = \frac{\partial^2 \tilde{p}_n}{\partial x^2} + \frac{\partial^2 \tilde{p}_n}{\partial z^2} = 0. \quad (2.11)$$

It is now useful to expand each Fourier component $\tilde{p}_n(x, z)$ in the infinite x -direction as $\sin x$ such that the y -average implies,

$$\tilde{p}_n = \hat{p}_n(z) \sin x, \quad (2.12a)$$

$$\langle \tilde{u}_n \rangle = \hat{u}_n = \frac{i\beta_n}{\xi_n} \hat{p}_n \cos x, \quad \langle \tilde{w}_n \rangle = \hat{w}_n = \frac{i\beta_n}{\xi_n} \frac{\partial \hat{p}_n}{\partial z} \sin x. \quad (2.12b)$$

Replacing (2.12a) in (2.11) leads to

$$\left(\frac{\partial^2}{\partial z^2} - 1 \right) \hat{p}_n = 0, \quad (2.13)$$

which admits the solution form

$$\hat{p}_n = c_1 \cosh z + c_2 \sinh z. \quad (2.14)$$

The presence of a solid bottom imposes that $\hat{w}_n = 0$ and, therefore, that $\partial \hat{p}_n / \partial z = 0$, at a non-dimensional fluid depth $z = -hk$, hence giving

$$\hat{p}_n = c_1 [\cosh z + \tanh kh \sinh z]. \quad (2.15)$$

Let us now invoke the linearized kinematic boundary condition

$$\frac{\partial \eta}{\partial t} = w. \quad (2.16)$$

Note that free surface elevation, $\eta'(x', y', t')$, has been rescaled by the forcing amplitude a , i.e. $\eta'/a = \eta$, and represents the projection of the bottom of the transverse concave meniscus on the xz -plane of figure 1(a). Moreover, by recalling the Floquet ansatz (2.6a)-(2.6b) (with $\mu_F = 0$), here specified for the interface, we get an equation for each Fourier component n ,

$$\eta = \sum_{n=-\infty}^{+\infty} \tilde{\eta}_n e^{i\xi_n t} \quad \longrightarrow \quad \forall n : \quad i\xi_n \tilde{\eta}_n = \tilde{w}_n. \quad (2.17)$$

Expanding $\tilde{\eta}_n$ in the x -direction as $\sin x$ and averaging in y , i.e. $\langle \tilde{\eta}_n \rangle = \hat{\eta}_n \sin x$, leads to

$$i\xi_n \hat{\eta}_n = \hat{w}_n = \frac{i\beta_n}{\xi_n} \frac{\partial \hat{p}_n(z=0)}{\partial z} = \frac{i\beta_n}{\xi_n} c_1 \tanh kh \quad \longrightarrow \quad c_1 = \frac{\xi_n^2}{\beta_n} \frac{\hat{\eta}_n}{\tanh kh}. \quad (2.18)$$

Lastly, we consider the linearized dynamic condition (or linearized normal stress), evaluated at $z' = \eta'$ and where the term associated with the curvature of the free surface appears,

$$-p' + \rho G(t') \eta' + 2\mu \frac{\partial w'}{\partial z'} - \gamma \left. \frac{\partial \kappa'}{\partial \eta'} \right|_{\eta'} = 0. \quad (2.19)$$

In (2.19), $\partial \kappa' / \partial \eta'$ represents the first-order variation of the curvature associated with the small perturbation η' . Capillary force in the x -direction is only important at large enough wavenumbers, although the associated term can be retained in the analysis in order to retrieve the dispersion relation for capillary-gravity waves (Li *et al.* 2019). On the other hand, the small gap of Hele-Shaw cells is such that surface tension effects in the narrow y -direction are strongly exacerbated. In general, the curvature can be divided into two parts (Saffman & Taylor 1958; Chuoke *et al.* 1959):

$$\kappa'(\eta') = \frac{\partial}{\partial x'} \left(\frac{\partial_{x'} \eta'}{\sqrt{1 + (\partial_{x'} \eta')^2}} \right) + \frac{2}{b} \cos \theta, \quad (2.20)$$

where the first term indicates the principal radius of curvature and the second term represents the out-of-plane curvature of the meniscus (see figure 1(a)). A common treatment of Hele-Shaw cells assumes the out-of-plane interface shape to be semicircular (Saffman & Taylor 1958; McLean & Saffman 1981; Park & Homsy 1984; Afkhami & Renardy 2013). Nevertheless, laboratory observations have unveiled that liquid oscillations in Hele-Shaw cells experience an up-and-down driving force with θ constantly changing (Jiang *et al.* 2004), hence giving rise to a dynamic contact angle. Here, as in Li *et al.* (2019), we use the following model (Hamraoui *et al.* 2000) to evaluate the cosine of the dynamic contact angle θ as

$$\cos \theta = 1 - \frac{M}{\mu} Ca = 1 - \frac{M w'}{\gamma} \quad (2.21)$$

where $Ca = \mu w' / \gamma$ is the Capillary number defined using the vertical contact line velocity $w' = \partial \eta' / \partial t'$. The friction coefficient M , sometimes referred to as mobility parameter M (Xia & Steen 2018), can be interpreted in the framework of molecular kinetics theory (O. V. Voinov 1976; Hocking 1987; Blake 1993, 2006; Johansson & Hess 2018), but here, in the same spirit of Li *et al.* (2019), we simply view this coefficient as a constant phenomenological fitting parameter that defines the energy dissipation rate per unit length of the contact line.

By combining equations (2.20)-(2.21) and taking their first-order curvature variation applied to the small perturbation, one can express

$$-\gamma \left. \frac{\partial \kappa'}{\partial \eta'} \right|_{\eta'} = -\gamma \frac{\partial^2 \eta'}{\partial x'^2} + \frac{2M}{b} \frac{\partial \eta'}{\partial t'}. \quad (2.22)$$

After turning to non-dimensional quantities using the scaling in (2.4), equations (2.19) reads

$$-\Omega^2 p + g\eta - \frac{\gamma}{\rho} k^2 \frac{\partial^2 \eta}{\partial x^2} + \frac{2M}{\rho b} \Omega \frac{\partial \eta}{\partial t} = a\Omega^2 \cos \Omega t' \eta, \quad (2.23)$$

where the viscous stress term has been eliminated, as it is negligible compared to the others.

With introduction of the Floquet ansatz (2.6b)-(2.17) and by recalling the x -expansion of the interface and pressure as $\sin x$, the averaged normal stress equations become

$$\forall n : \quad -\Omega^2 \hat{p}_n + i(\xi_n \Omega) \frac{2M}{\rho b} \hat{\eta}_n + \left(1 + \frac{\gamma}{\rho g} k^2 \right) g \hat{\eta}_n = \frac{a\Omega^2}{2g} g (\hat{\eta}_{n-1} + \hat{\eta}_{n+1}). \quad (2.24)$$

where the decomposition $\cos \Omega t' = (e^{i\Omega t'} + e^{-i\Omega t'}) / 2 = (e^{it} + e^{-it}) / 2$ has also been used. Equations (2.15) and (2.18) are finally used to express the dynamic equation as a function of the non-dimensional averaged interface only,

$$-\frac{(\xi_n \Omega)^2}{\beta_n} \hat{\eta}_n + i (\xi_n \Omega) \frac{2M}{\rho b} k \tanh kh \hat{\eta}_n + (1 + \Gamma) g k \tanh kh \hat{\eta}_n = \frac{g k \tanh kh}{2} f (\hat{\eta}_{n-1} + \hat{\eta}_{n+1}), \quad (2.25)$$

with the auxiliary variables $f = a\Omega^2/g$ and $\Gamma = \gamma k^2/\rho g$, such that $(1 + \Gamma) g k \tanh kh = \omega_0^2$, the well-known dispersion relation for capillary-gravity waves (Lamb 1993).

As in the present form the interpretation of coefficient β_n does not appear straightforward, it is useful to define the damping coefficients

$$\sigma_n = \sigma_{BL} + \sigma_{CL}, \quad \sigma_{BL} = \chi_n \frac{\nu}{b^2}, \quad \sigma_{CL} = \frac{2M}{\rho b} k \tanh kh, \quad (2.26a)$$

where χ_n is used to help rewriting $\frac{1}{\beta_n} = 1 - i \frac{\delta_n^2}{2} \chi_n$,

$$\chi_n = i \frac{2}{\delta_n^2} \left(\frac{1 - \beta_n}{\beta_n} \right) = 12 \left[\frac{i}{6\delta_n^2} \left(\frac{\frac{2\delta_n}{1+i} \tanh \frac{1+i}{2\delta_n}}{1 - \frac{2\delta_n}{1+i} \tanh \frac{1+i}{2\delta_n}} \right) \right]. \quad (2.26b)$$

These auxiliary definitions allows one to express (2.25) as

$$-(\xi_n \Omega)^2 \hat{\eta}_n + i (\xi_n \Omega) \sigma_n \hat{\eta}_n + \omega_0^2 \hat{\eta}_n = \frac{\omega_0^2}{2(1 + \Gamma)} f [\hat{\eta}_{n+1} + \hat{\eta}_{n-1}]. \quad (2.27)$$

or, equivalently,

$$\frac{2(1 + \Gamma)}{\omega_0^2} [-(n\Omega + \alpha)^2 + i(n\Omega + \alpha) \sigma_n + \omega_0^2] \hat{\eta}_n = f [\hat{\eta}_{n+1} + \hat{\eta}_{n-1}]. \quad (2.28)$$

Subscripts *BL* and *CL* in (2.26a) denote, respectively, the boundary layers and contact line contributions to the total damping coefficient σ_n .

At the end of this long mathematical derivation, the main result is the modified damping coefficient σ_n . Since the boundary layer contribution, σ_{BL} depends on the n th Fourier component, the overall damping, σ_n , is mode dependent and its value is different for each specific n th parametric resonant tongue considered. This is in stark contrast with the standard Darcy approximation, where σ_{BL} is the same for each resonance and amounts to $12\nu/b^2$. In our model, the case of $\alpha = 0$ with $n = 0$ constitutes a peculiar case, as $\xi_n = \xi_0 = 0$ and $\delta_0 \rightarrow +\infty$. In such a situation, $F_0(y)$ tends to the steady Poiseuille profile, so that we take $\chi_0 = 12$.

Similarly to Kumar & Tuckerman (1994), equation (2.28) is rewritten as

$$A_n \hat{\eta}_n = f [\hat{\eta}_{n+1} + \hat{\eta}_{n-1}], \quad (2.29)$$

with

$$A_n = \frac{2(1 + \Gamma)}{\omega_0^2} \left(-(n\Omega + \alpha)^2 + i(n\Omega + \alpha) \sigma_n + \omega_0^2 \right) = A_n^r + iA_n^i \in \mathbb{C} \quad (2.30)$$

The non-dimensional amplitude of the external forcing, $f = a\Omega^2/g$ appears linearly, therefore (2.29) can be considered to be a generalized eigenvalue problem

$$\mathbf{A} \hat{\eta} = f \mathbf{B} \hat{\eta}, \quad (2.31)$$

with eigenvalues f and eigenvectors whose components are the real and imaginary parts of $\hat{\eta}_n$. See Kumar & Tuckerman (1994) for the structure of matrices \mathbf{A} and \mathbf{B} .

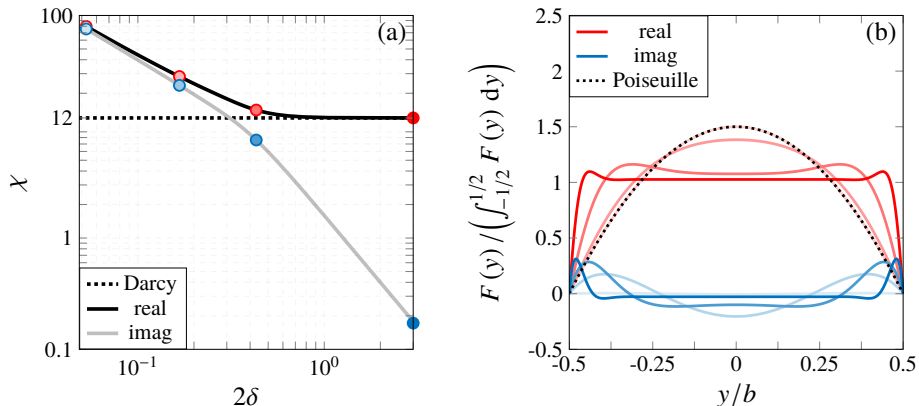


Figure 2: (a) Real and imaginary parts of the complex auxiliary coefficient $\chi = \chi_r + i\chi_i$ versus twice the non-dimensional Stokes boundary layer thickness δ . The horizontal black dotted line indicates the constant value 12 given by the Darcy approximation. (b) Normalized profile $F(y)$ (Womersley profile) for different $\delta = b^{-1}\sqrt{2\nu/\xi\Omega}$, whose values are specified by the filled circles in (a) with matching colors. The Poiseuille profile is also reported for completeness. In drawing these figures we let the oscillation frequency of the wave, $\xi\Omega$, free to assume any value, but we recall that the parameter ξ can only assume discrete values, and so do χ and $F(y)$.

For one frequency forcing we use a truncation number $N = 10$, which produces $2(N+1) \times 2(N+1) = 22 \times 22$ matrices. Eigen-problem (2.31) is then solved in Matlab using the built-in function *eigs*, by asking for the eigenvalue (or few eigenvalues) with the smallest real part.

Figure 3 shows the results of this procedure for one of the configurations considered by Li *et al.* (2019) and neglecting the dissipation associated with the contact line motion, i.e. $M = 0$. In each panel, associated with a fixed forcing frequency, the black regions correspond to the unstable Faraday tongues computed using $\sigma_{BL} = 12\nu/b^2$ as given by Darcy's approximation, whereas the red regions are the unstable tongues computed with the modified $\sigma_{BL} = \chi_n\nu/b^2$. At a forcing frequency 4 Hz the first sub-harmonic tongues computed using the two models essentially overlap. Yet, successive resonances display an increasing departure from Darcy's model due to the newly introduced complex coefficient σ_n . Particularly, the real part of χ_n is responsible for the higher onset acceleration, while the imaginary part is expected to act as a detuning term, which shifts the resonant wavenumbers k .

2.2. Asymptotic approximations

The main result of this analysis consists in the derivation of the modified damping coefficient $\sigma_n = \sigma_{n,r} + i\sigma_{n,i}$ associated with each parametric resonance. Aiming at better elucidating how this modified complex damping influences the stability properties of the system, we would like to derive in this section an asymptotic approximation, valid in the limit of small forcing amplitudes, damping and detuning, of the first sub-harmonic (SH1) and harmonic (H1) Faraday tongues.

Unfortunately, the dependence of σ_n on the parametric resonance considered and, more specifically, on the n th Fourier component, does not allow one to convert (2.27), expressed in a discrete frequency domain, back into the continuous temporal domain. By keeping this in mind, we can still imagine fixing the value of σ_n to that corresponding to the parametric resonance of interest, e.g. σ_0 (with $n = 0$ and $\xi_0\Omega = \Omega/2$) for SH1 or σ_1 (with $n = 1$ and $\xi_1\Omega = \Omega$) for H1. By considering then that for the SH1 and H1 tongues, the system responds in time as $\exp(i\Omega t/2)$ and $\exp(i\Omega t)$, respectively, we can recast, for these two

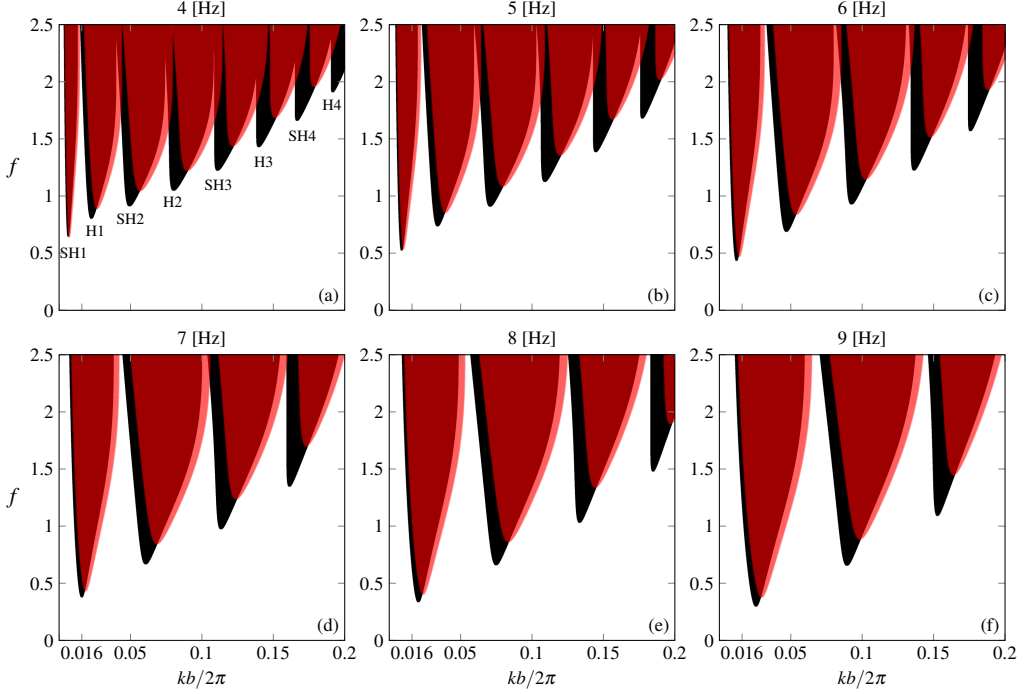


Figure 3: Faraday tongues computed via Floquet analysis at different fixed driving frequencies (reported on the top of each panel). Black regions correspond to the unstable Faraday tongues computed using $\sigma_{BL} = 12\nu/b^2$ as in the standard Darcy approximation, whereas red regions are the unstable tongues computed with the present modified $\sigma_{BL} = \chi_n\nu/b^2$. For this example, we consider ethanol 99.7% (see table 1) in a Hele-Shaw cell of gap size $b = 2$ mm filled to a depth $h = 60$ mm. f denotes the non-dimensional forcing acceleration, $f = a\Omega^2/g$, with dimensional forcing amplitude a and angular frequency Ω . For plotting, we define a small scale-separation parameter $\epsilon = kb/2\pi$ and we arbitrarily set its maximum acceptable value to 0.2. Contact line dissipation is not included, i.e. $M = \sigma_{CL} = 0$. SH stands for sub-harmonic, whereas H stands for harmonic.

specific cases, equations (2.27) into a damped Mathieu equation (Benjamin & Ursell 1954; Kumar & Tuckerman 1994; Müller *et al.* 1997)

$$\frac{\partial^2 \hat{\eta}}{\partial t'^2} + \hat{\sigma}_n \frac{\partial \hat{\eta}}{\partial t'} + \omega_0^2 \left(1 - \frac{f}{1+\Gamma} \cos \Omega t' \right) \hat{\eta} = 0. \quad (2.32)$$

with either $\hat{\sigma}_n = \sigma_0$ (SH1) or $\hat{\sigma}_n = \sigma_1$ (H1) and where one can recognize that $-(\xi_n \Omega)^2 \hat{\eta} \leftrightarrow \partial^2 \hat{\eta} / \partial t'^2$ and $i(\xi_n \Omega) \hat{\eta} \leftrightarrow \partial \hat{\eta} / \partial t'$. Asymptotic approximations can be then computed by expanding asymptotically the interface as $\hat{\eta} = \hat{\eta}_0 + \epsilon \hat{\eta}_1 + \epsilon^2 \hat{\eta}_2 + \dots$, with ϵ a small parameter $\ll 1$.

2.2.1. First sub-harmonic tongue

As anticipated above, when looking at the first or fundamental sub-harmonic tongue (SH1), one should take $\hat{\sigma}_n \rightarrow \sigma_0$ (with $\xi_0 \Omega = \Omega/2$), which is assumed small of order ϵ . The forcing amplitude f is assumed of order ϵ as well. Furthermore, a small detuning $\sim \epsilon$, such that $\Omega = 2\omega_0 + \epsilon\lambda$, is also considered, and, in the spirit of the multiple timescale analysis, a slow time scale $T = \epsilon t'$ (Nayfeh 2008) is introduced. At leading order, the solution reads $\hat{\eta}_0 = A(T) e^{i\omega_0 t'} + c.c.$, with *c.c.* denoting the complex conjugate part. At the second order

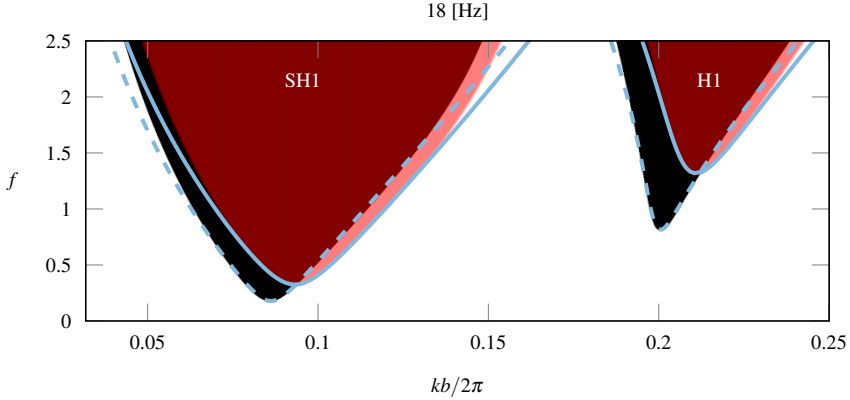


Figure 4: First sub-harmonic and harmonic Faraday tongues at a driving frequency $1/T = 18$ Hz for the same configuration of figure 3. Black and red regions show unstable tongues computed via Floquet analysis by using, respectively, $\sigma_{BL} = 12\nu/b^2$ and the modified $\sigma_{BL} = \chi_1\nu/b^2$ from the present model. Dashed and solid light-blue lines correspond to the asymptotic approximations according to (2.34) and (2.37).

in ϵ , the imposition of a solvability condition necessary to avoid secular terms prescribes the amplitude $B(T) = A(T) e^{-i\lambda T/2}$ to obey the following amplitude equation

$$\frac{dB}{dT} = -\frac{\sigma_0}{2}B - i\frac{\lambda}{2}B - i\frac{\omega_0}{4(1+\Gamma)}f\bar{B}. \quad (2.33)$$

Turning to polar coordinates, i.e. $B = |B|e^{i\Phi}$, keeping in mind that $\sigma_0 = \sigma_{0,r} + i\sigma_{0,i}$ and looking for stationary solutions with $|B| \neq 0$ (we skip the straightforward mathematical steps), one ends up with the following approximation for the marginal stability boundaries associated with the first sub-harmonic Faraday tongue

$$\left(\frac{\Omega + \sigma_{0,i}}{2\omega_0} - 1\right) = \pm \frac{1}{4(1+\Gamma)} \sqrt{f^2 - \frac{4\sigma_{0,r}^2(1+\Gamma)^2}{\omega_0^2}}, \quad (2.34)$$

whose onset acceleration value, $\min f_{1,SH}$, amounts to

$$\min f_{SH1} = 2\sigma_{0,r} \sqrt{\frac{1+\Gamma}{gk \tanh kh}} \approx 2\sigma_{0,r} \sqrt{\frac{1}{g} \left(\frac{1}{k} + \frac{\gamma}{\rho g} k\right)}, \quad (2.35)$$

Note that the final approximation on the right-hand-side of (2.35) only holds if $kh \gg 1$, so that $\tanh kh \approx 1$ (deep water regime). Given that $\chi_{0,r} > 12$ and $\chi_{0,i} > 0$ always, the asymptotic approximation (2.35), in its range of validity, suggests that Darcy's model underestimates the sub-harmonic stability threshold. Moreover, from (2.34), the critical wavenumber k , associated with $\min f_{SH1}$, would correspond to that prescribed by the Darcy approximation but at an effective forcing frequency $\Omega + \sigma_{0,i} = 2\omega_0$ instead of at $\Omega = 2\omega_0$. This explains why the modified tongues appear shifted towards higher wavenumbers. These observations are well visible in figure 4.

2.2.2. First harmonic tongue

By analogy with §2.2.1, an analytical approximation of the first harmonic tongue (H1) can be provided. In the same spirit of Rajchenbach & Clamond (2015), we adapt the asymptotic

Liquid	μ [mPa s]	ρ [kg/m ³]	γ [N/m]	M [Pa s]
ethanol 99.7%	1.096	785	0.0218	0.04
ethanol 70.0%	2.159	835	0.0234	0.0485
ethanol 50.0%	2.362	926	0.0296	0.07

Table 1: Characteristic fluid parameters for the three ethanol-water mixtures considered in this study. Data for the pure ethanol and ethanol-water mixture (50%) are taken from Li *et al.* (2019). The value of the friction parameter M for ethanol-70% is fitted from the experimental measurements reported in §4, but lies well within the range of values used by Li *et al.* (2019) and agrees with the linear trend displayed in figure 5 of Hamraoui *et al.* (2000).

scaling such that f is still of order ϵ , but $T = \epsilon^2$, $\hat{\sigma}_n = \sigma_1 \sim \epsilon^2$ (with $\xi_1 \Omega = \Omega$) and $\Omega = \omega_0 + \epsilon^2 \lambda$. Pursuing the expansion up to ϵ^2 -order, with $\hat{\eta}_0 = A(T) e^{i\omega_0 t'} + c.c.$ and $B(T) = A(T) e^{-i\lambda T}$, will provide the amplitude equation

$$\frac{dB}{dT} = -\frac{\sigma_1}{2} B - i\lambda B - i \frac{\omega_0}{8(1+\Gamma)^2} f^2 \bar{B} + i \frac{\omega_0}{12(1+\Gamma)^2} f^2 B. \quad (2.36)$$

The approximation for the marginal stability boundaries derived from (2.36) takes the form

$$\left(\frac{\Omega + \sigma_{1,i}/2}{\omega_0} - 1 \right) = \frac{f^2}{12(1+\Gamma)^2} \pm \frac{1}{8(1+\Gamma)^2} \sqrt{f^4 - \left(\frac{4\sigma_{1,r}(1+\Gamma)^2}{\omega_0} \right)^2} \quad (2.37)$$

with a minimum onset acceleration, $\min f_{1H}$

$$\min f_H = 2\sqrt{\sigma_{1,r}} \left(\frac{(1+\Gamma)^3}{gk \tanh kh} \right)^{1/4} \approx 2\sqrt{\sigma_{1,r}} \frac{1}{g^{1/4}} \left(\frac{1}{k^{1/3}} + \frac{\gamma}{\rho g} k^{5/3} \right)^{3/4}, \quad (2.38)$$

and where, as before, the final approximation on the right-hand side is only valid in the deep water regime. Similarly to the sub-harmonic case, the critical wavenumber k corresponds to that prescribed by the Darcy approximation but at an effective forcing frequency $\Omega + \sigma_{1,i}/2 = \omega_0$ instead of at $\Omega = \omega_0$ and the onset acceleration is larger than that predicted from the Darcy approximation (as $\chi_{1,r} > 12$).

2.3. Comparison with experiments by Li *et al.* (2019)

Results presented so far were produced by assuming the absence of contact line dissipation, i.e. coefficient M was set to $M = 0$, so that $\sigma_{CL} = 0$. In this section, we reintroduce such a dissipative contribution and we compare our theoretical predictions with a set of experimental measurements reported by Li *et al.* (2019), using the values they have proposed for M . This comparison, shown in figure 5, is outlined in terms of non-dimensional minimum onset acceleration, $\min f = \min f_{SH1}$, versus driving frequency. These authors performed experiments in two different Hele-Shaw cells of length $l = 300$ mm, fluid depth $h = 60$ mm and gap-size $b = 2$ mm or $b = 5$ mm. Two fluids, whose properties are reported in table 1, were used: ethanol 99.7% and ethanol 50%. The empty squares in figure 5 are computed via Floquet stability analysis (2.31) using the Darcy approximation for $\sigma_{BL} = 12\nu/b^2$ and correspond to the theoretical prediction by Li *et al.* (2019), while the colored triangles are computed using the corrected $\sigma_{BL} = \chi_n \nu/b^2$. Although the trend is approximately the same, the Darcy approximation underestimates the onset acceleration with respect to the

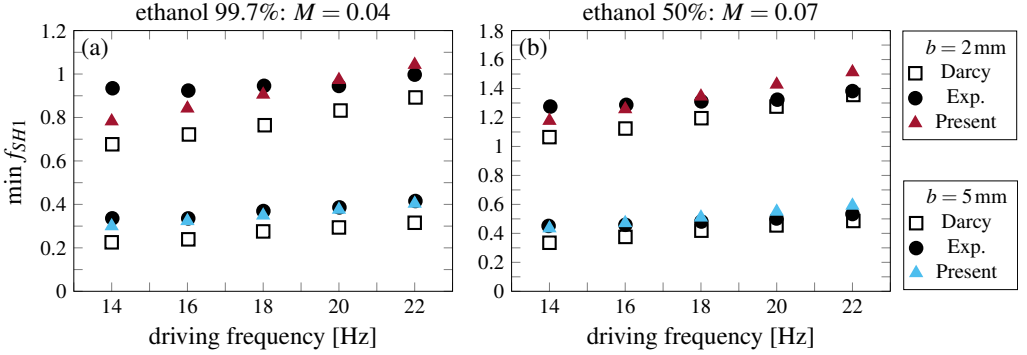


Figure 5: Sub-harmonic instability onset, $\min f$, versus forcing frequency. Comparison between theoretical data (empty squares: standard Darcy model, $\sigma_{BL} = 12\nu/b^2$; colored triangles: present model, $\sigma_{BL} = \chi_n\nu/b^2$) and experimental measurements by Li *et al.* (2019). The values of the mobility parameter M here employed are reported in the figure.

present model, which overall compares better with the experimental measurements (black-filled circles). Some disagreement still exists, especially at smaller cell gaps, i.e. $b = 2$ mm, where surface tension effects are even larger. This is likely attributable to an imperfect phenomenological contact line model (Bongarzone *et al.* 2021, 2022), whose definition falls beyond the scope of this work. Yet, this comparison shows how the modifications introduced by the present model contribute to closing the gap between theoretical Faraday onset estimates and these experiments.

3. The case of thin annuli

We now consider the case of a thin annular container, whose nominal radius is R and the actual inner and outer radii are $R - b/2$ and $R + b/2$, respectively (see the sketch in figure 1(b)). In the limit of $b/R \ll 1$, the wall curvature is negligible and the annular container can be considered a Hele-Shaw cell. The following change of variable for the radial coordinate, $r' = R + y' = R(1 + y'/R)$ with $y' \in [-b/2, b/2]$, will be useful in the rest of the analysis. As in §2, we first linearize around the rest state. Successively, we introduce the following non-dimensional quantities,

$$r = \frac{r'}{R}, \quad y = \frac{y'}{b}, \quad z = \frac{z'}{R}, \quad u = \frac{u'_\varphi}{a\Omega}, \quad v = \frac{u'_r}{a\Omega(b/R)}, \quad w = \frac{u'_z}{a\Omega^2}, \quad p = \frac{p'}{\rho Ra\Omega^2}. \quad (3.1)$$

It follows that, at leading order, $r = R(1 + yb/R) \sim R \rightarrow 1/r = 1/(R(1 + yb/R)) \sim 1/R$ but $\partial/\partial r = (R/b)\partial/\partial y \sim b/R \gg 1$. With this scaling and introducing the Floquet ansatz (2.6a)-(2.6b), one obtains the following simplified governing equations,

$$\frac{\partial \tilde{u}_n}{\partial \varphi} + \frac{\partial \tilde{v}_n}{\partial y} + \frac{\partial \tilde{w}_n}{\partial z} = 0, \quad (3.2a)$$

$$i\tilde{u}_n = -\frac{1}{\xi_n} \frac{\partial \tilde{p}_n}{\partial \varphi} + \frac{\delta_n^2}{2} \frac{\partial^2 \tilde{u}_n}{\partial y^2}, \quad i\tilde{w}_n = -\frac{1}{\xi_n} \frac{\partial \tilde{p}_n}{\partial z} + \frac{\delta_n^2}{2} \frac{\partial^2 \tilde{w}_n}{\partial y^2} \quad \text{or} \quad \tilde{\mathbf{u}}_n = \frac{i}{\xi_n} \nabla \tilde{p}_n F_n(y), \quad (3.2b)$$

which are fully equivalent to those for the case of conventional rectangular cells if the transformation $\varphi \rightarrow x$ is introduced. Averaging the continuity equation with the imposition

of the no-penetration condition at $y = \mp 1/2$, $v(\mp 1/2)$, eventually leads to

$$\nabla^2 \tilde{p}_n = \frac{\partial^2 \tilde{p}_n}{\partial z^2} + \frac{\partial^2 \tilde{p}_n}{\partial \varphi^2}, \quad (3.3)$$

identically to (2.11). Expanding \tilde{p}_n in the azimuthal direction as $\tilde{p}_n = \hat{p}_n \sin m\varphi$, with m the azimuthal wavenumber, provides

$$\left(\frac{\partial^2}{\partial z^2} - m^2 \right) \hat{p}_n = 0 \quad \longrightarrow \quad \hat{p}_n = c_1 \cosh mz + c_2 \sinh mz, \quad (3.4)$$

and the no-penetration condition at the solid bottom located at $z = -h/R$, $\hat{w}_n = \partial_z \hat{p}_n = 0$, prescribes

$$\hat{p}_n = c_1 (\cosh mz + \tanh mh/R \sinh mz). \quad (3.5)$$

Although so far the rectangular and the annular cases are indistinguishable from each other, here it is crucial to observe that the axisymmetric container geometry translates into a periodicity condition according to which

$$\sin(-m\pi) = \sin(m\pi) \quad \longrightarrow \quad \sin m\pi = 0, \quad (3.6)$$

and that always imposes the azimuthal wavenumber to be an integer. In other words, in contradistinction with the case of §2, where the absence of lateral wall ideally allows for any wavenumber k , here we have $m = 0, 1, 2, 3, \dots \in \mathbb{N}$.

By repeating the calculations outlined in §2, one ends up with the very same equation (2.28) (and subsequent (2.29)-(2.31)), but where ω_0 obeys to the *quantized* dispersion relation

$$\omega_0^2 = \left(\frac{g}{R} m + \frac{\gamma}{\rho R^3} m^3 \right) \tanh m \frac{h}{R} = (1 + \Gamma) \frac{g}{R} m \tanh m \frac{h}{R}. \quad (3.7)$$

with $\Gamma = \gamma m^2 / \rho g R^2$. In this context, a representation of Faraday's tongues in the forcing frequency-amplitude plane appears most natural, as each parametric tongue will correspond to a fixed wavenumber m . Consequently, instead of fixing Ω and varying the wavenumber, here we solve (2.31) by fixing m and varying Ω .

3.1. Floquet analysis and asymptotic approximation

The results from this procedure are reported in figure 6, where, as in figure 3, the black regions correspond to the unstable tongues obtained according to the standard gap-averaged Darcy model, while the red ones are computed using the corrected $\sigma_{BL} = \chi_n v / b^2$. The Faraday threshold is represented in terms of forcing acceleration (panels (a) and (b)) and forcing amplitude (panels (c) and (d)). In figure 6(a)-(c) no contact line model is included, whereas in (b)-(d) a mobility parameter $M = 0.0485$ is accounted for. This specific value for M will be used in the next section when comparing the theory with dedicated experiments. The regions with the lowest thresholds in each panel are sub-harmonic tongues associated with modes from $m = 1$ to 14. For the case with $M \neq 0$, the instability onset acceleration associated with each wavenumber m appears to follow a linear trend, as already reported in figure 5.

In general, the present model gives a higher instability threshold, consistent with the results reported in the previous section. However, the tongues are here shifted to the left. This apparent opposite correction is a natural consequence of the different representations: varying wavenumber at a fixed forcing frequency (as in figure 3) versus varying forcing frequency at a fixed wavenumber (figure 6).

The asymptotic approximation for the sub-harmonic onset acceleration, adapted to this

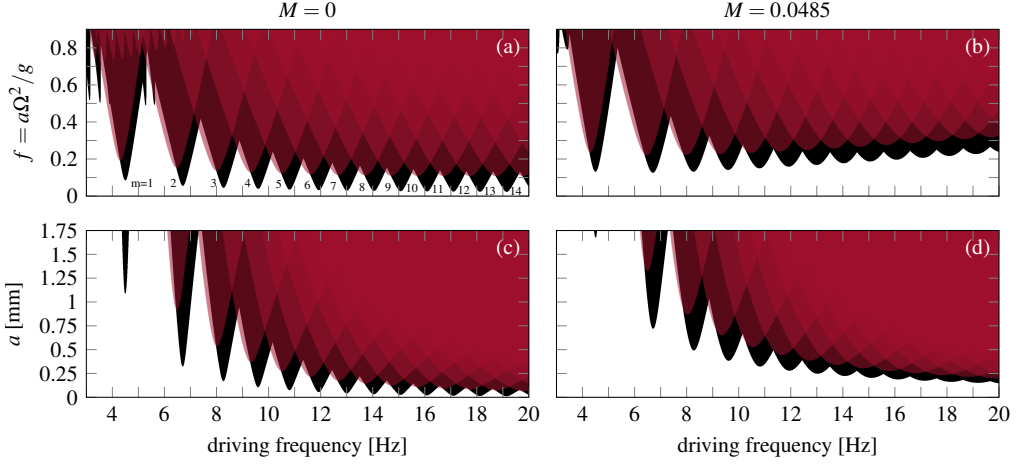


Figure 6: Faraday tongues computed via Floquet analysis (2.31) at different fixed azimuthal wavenumber m and varying the driving frequency. (a)-(b) Faraday thresholds in terms of forcing acceleration $f = a\Omega^2/g$; (c)-(d) Threshold in terms of forcing amplitude a . Black regions correspond to the unstable Faraday tongues computed using $\sigma_{BL} = 12\nu/b^2$, whereas red regions are the unstable tongues computed with the present modified $\sigma_{BL} = \chi_n\nu/b^2$. The fluid parameters used here correspond to those given in table 1 for ethanol 70%. The gap-size is set to $b = 7$ mm, the fluid depth to $h = 65$ mm and the nominal radius to $R = 44$ mm. Contact line dissipation is included in (b) and (d) by accounting for a mobility coefficient $M = 0.0485$. The regions with the lowest thresholds in each panel are sub-harmonic tongues associated with modes from $m = 1$ to 14.

case from (2.34) in §2.2.1,

$$f_{SH1} = 2\sqrt{(1+\Gamma) \frac{\sigma_{0,r}^2}{(g/R) m \tanh mh/R} + 4(1+\Gamma)^2 \left(\frac{\Omega + \sigma_{0,i}}{2\omega_0} - 1\right)^2}, \quad (3.8)$$

with

$$\min f_{SH1} = 2\sigma_{0,r} \frac{1+\Gamma}{\omega_0} = 2\sigma_{0,r} \sqrt{\frac{1+\Gamma}{(g/R) m \tanh mh/R}} \approx 2\sigma_{0,r} \sqrt{\frac{R}{g} \left(\frac{1}{m} + \frac{\gamma}{\rho g R^2} m\right)}, \quad (3.9)$$

helps us indeed in rationalizing the influence of the modified complex damping coefficient.

The apparent opposite shift shown in figure 6 in comparison to that displayed in figure 3, is clarified by the asymptotic relation (3.8) and, particularly by the term $\left(\frac{\Omega + \sigma_{0,i}}{2\omega_0} - 1\right)$. In §2, the analysis is based on a fixed forcing frequency, while the wavenumber k and, hence, the natural frequency ω_0 , are let free to vary. The first sub-harmonic Faraday tongue occurs when $\Omega + \sigma_{0,i} \approx 2\omega_0$. Since Ω is fixed and $\sigma_{0,i} > 0$, $\Omega + \sigma_{0,i} > \Omega$ such that ω_0 and therefore k have to increase in order to satisfy the relation. On the other hand, if the wavenumber m and, hence, ω_0 are fixed as in this section, then $2\omega_0 - \sigma_{0,i} < 2\omega_0$ and the forcing frequency around which the sub-harmonic resonance is centered, decreases of a contribution $\sigma_{0,i}$, which introduces a frequency detuning responsible for the negative frequency shift displayed in figure 6.

3.2. Discussion on the system's spatial quantization

A first aspect that needs to be better discussed is the frequency-dependence of the damping coefficient σ_n associated with each Faraday's tongue. In the case of horizontally infinite cells, the most natural description for investigating the system's stability properties is in the (k, f) plane for a fixed forcing angular frequency Ω (Kumar & Tuckerman 1994). According to our model, the oscillating system's response occurring within each tongue is characterized by a Stokes boundary layer thickness $\delta_n = \sqrt{2\nu/(n\Omega + \alpha)}/b$. For instance, let us consider sub-harmonic resonances with $\alpha = \Omega/2$. As Ω is fixed (see any sub-panel of figure 3), each unstable region sees a constant δ_n (with $n = 0, 1, 2, \dots$) and hence a constant damping σ_n .

On the other hand, in the case of quantized wavenumber as for the annular cell of §3, the most suitable description is in the driving frequency-driving amplitude plane at fixed wavenumber m (see figure 6) (Batson *et al.* 2013). In this description, each sub-harmonic ($\alpha = \Omega/2$) or harmonic ($\alpha = \Omega$) n th tongue associated with a wavenumber m , sees a δ_n , and thus a σ_n , changing with Ω along the tongue itself.

Furthermore, it is important to realize that in a real lab-scale experiment, the horizontal size of rectangular cells is never actually infinite. It follows that if the analysis of §2 is restrained to horizontally finite cells of overall length l , then one must impose the no-penetration condition for u' at $x' = \pm l/2$, which would set the admissible wavenumbers to $k = m\pi/l$ only, with $m = 0, 1, 2, \dots \in \mathbb{N}$, thus completing the analogy with the annular configuration.

In such a case however, the solution form (2.9) prevents the no-slip condition for the in-plane xz -velocity components to be imposed (Viola *et al.* 2017). This always translates into an underestimation of the overall damping of the system in standard Hele-Shaw cells, although the sidewall contribution is expected to be negligible for sufficiently long cells.

On the other hand, the case of a thin annulus, by naturally filtering out this extra dissipation owing to the periodicity condition, offers a prototype configuration that can allow one to better quantify the correction introduced by the present gap-averaged model when compared to dedicated experiments, as outlined in the next section.

4. Experiments

4.1. Setup

The experimental apparatus, shown in figure 7, is very simple. We used a Plexiglas annular container of height 100 mm, nominal radius $R = 44$ mm and gap-size $b = 7$ mm, which is then filled to a depth $h = 65$ mm with ethanol 70% (see table 1 for the fluid properties). An air conditioning system helps in maintaining the temperature of the room at around 22° . The container is mounted on a loudspeaker VISATON TIW 360 8Ω placed on a flat table and connected to a wave generator TEKTRONIX AFG 1022, whose output signal is amplified using a wideband amplifier THURKBY THANDER WA301. The motion of the free surface is recorded with a digital camera NIKON D850 coupled with a 60mm f/2.8D lens and operated in slow motion mode, allowing for an acquisition frequency of 120 frames per second. A LED panel placed behind the apparatus provides back illumination of the fluid interface for better optimal contrast. The wave generator imposes a sinusoidal alternating voltage, $v = (V_{pp}/2) \cos(\Omega t')$, with Ω the angular frequency and V_{pp} the full peak-to-peak voltage. The response of the loudspeaker to this input translates into a vertical harmonic motion of the container, $a \cos(\Omega t')$, whose amplitude, a [mm], is measured with a chromatic confocal displacement sensor STI CCS PRIMA/CLS-MG20. This optical pen, which is placed around 2 cm (within the admissible working range of 2.5 cm) above the container and points at the top flat surface of the outer container's wall, can detect the time-varying distance between the fixed sensor and the oscillating container's surface with a sampling rate in the order of kHz

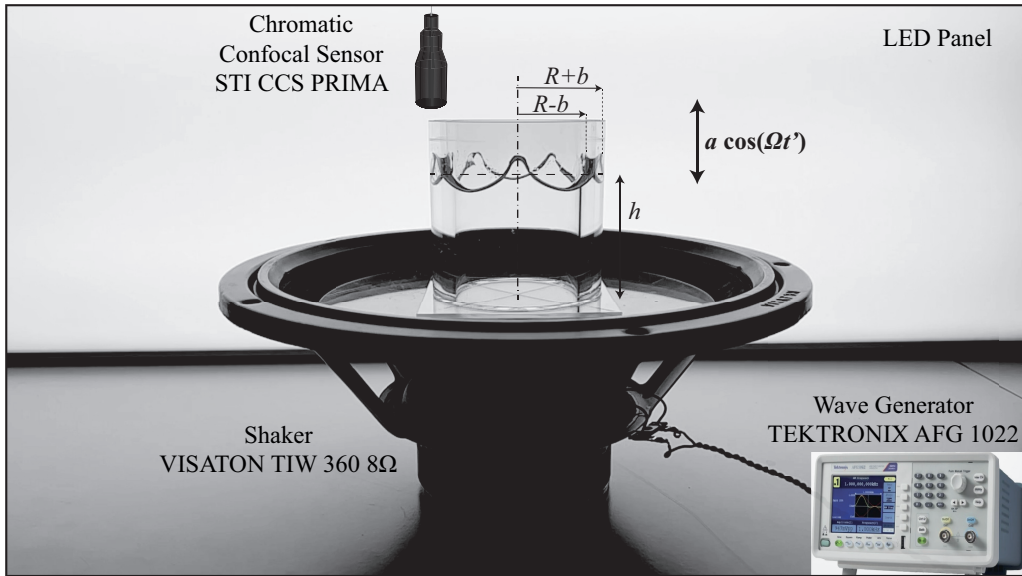


Figure 7: Photo of the experimental setup

and a precision of $\pm 1 \mu\text{m}$. Therefore, the pen can be used to obtain a very precise real-time value of a as the voltage amplitude V_{pp} and the frequency Ω are adjusted.

4.2. Identification of the accessible experimental range

Our simple setup put some constraints on the explorable experimental frequency range.

(i) First, we need to ensure that the loudspeaker's output translates into a vertical container's displacement following a sinusoidal time signal. To this end, the optical sensor is used to measure the container motion at different driving frequencies. These time signals are then fitted with a sinusoidal law. Figure 8 shows how below a forcing frequency of 8 Hz, the loudspeaker's output begins to depart from a sinusoidal signal. This check imposes a first lower bound on the explorable frequency range.

(ii) In addition, as Faraday waves only appear above a threshold amplitude, it is convenient to measure *a priori* the maximal vertical displacement a achievable. The loudspeaker response curve is reported in the bottom part of figure 8. A superposition of this curve with the predicted Faraday's tongues immediately identifies the experimental frequency range within which the maximal achievable a is larger than the predicted Faraday threshold so that standing waves are expected to emerge in our experiments. Assuming the herein proposed gap-averaged model (red regions) to give a good prediction of the actual instability onset, the experimental range explored in the next section is limited to approximately $\in [10.2, 15.6]$ Hz.

4.3. Procedure

Given the constraints discussed in §4.2, experiments have been carried out in a frequency range between 10.2 Hz and 15.6 Hz with a frequency step of 0.1 Hz. For each fixed forcing frequency, the Faraday threshold is determined as follows: the forcing amplitude a is set to the maximal value achievable by the loudspeaker, so as to quickly trigger the emergence of the unstable Faraday wave. The amplitude is then progressively decreased until the wave disappears and the surface becomes flat again.

More precisely, a first quick pass across the threshold is made to determine an estimate

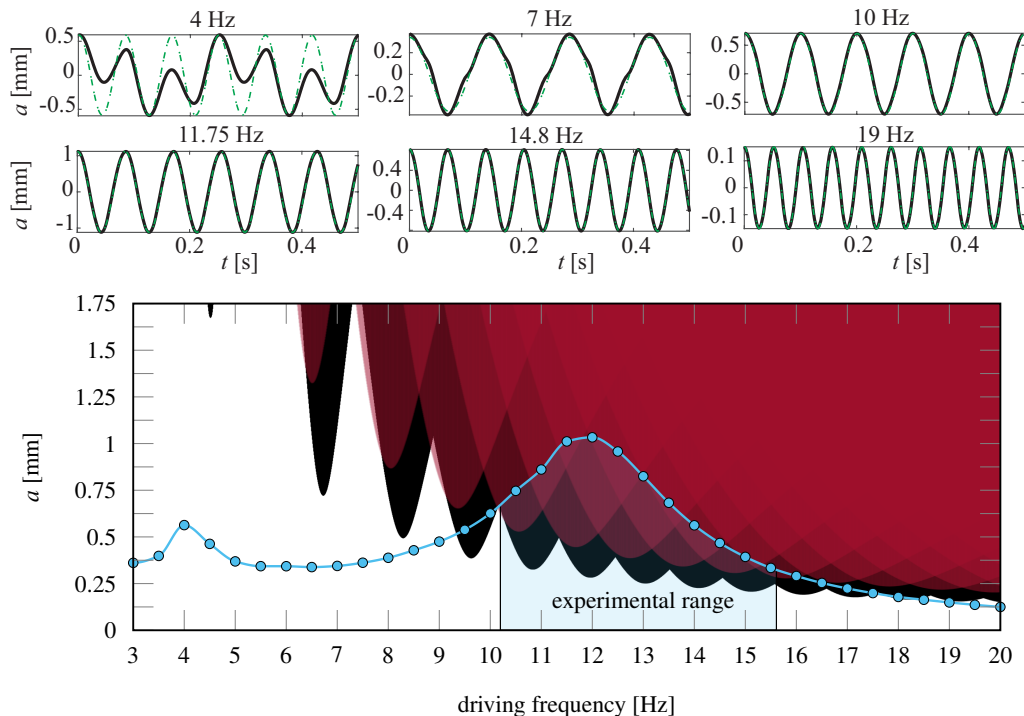


Figure 8: *Top*: vertical container displacement a versus time at different forcing frequencies. The black curves are the measured signal, while the green dash-dotted curves are sinusoidal fitting. Below a forcing frequency of 8 Hz, the loudspeaker's output begins to depart from a sinusoidal signal. *Bottom*: same as in figure 6(d): sub-harmonic Faraday tongues computed by accounting for contact line dissipation with a mobility parameter $M = 0.0485$. The light blue curve here superposed corresponds to the maximal vertical displacement a achievable with our setup. With this constraint, Faraday waves are expected to be observable only in the frequency range highlighted in blue.

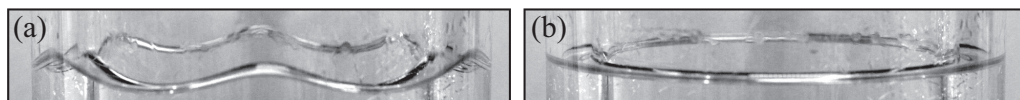


Figure 9: Free surface shape at a forcing frequency $1/T = 11.7$ Hz and corresponding to: (a) the lowest forcing amplitude value, $a = 0.4693$ mm, for which the $m = 6$ standing wave is present (the figure shows a temporal snapshot); (b) the largest forcing amplitude value, $a = 0.4158$ mm, for which the surface becomes flat and stable again. Despite the small forcing amplitude variation, the change in amplitude is large enough to allow for a visual inspection of the instability threshold with sufficient accuracy.

of the sought amplitude. A second pass is then made by starting again from the maximum amplitude and decreasing it. When we approach the value determined during the first pass, we perform finer amplitude decrements, and we wait several minutes between each amplitude change to ensure that the wave stably persists. We eventually identify two values: the last amplitude where the instabilities were present (see figure 9(a)) and the first one where the surface becomes flat again (see figure 9(b)). Two more runs following an identical procedure are then performed to verify the values previously found. Lastly, an average between the smallest unstable amplitude and the largest stable one gives us the desired threshold.

Once the threshold amplitude value is found for the considered frequency, the output of the wave generator is switched off, the frequency is changed, and the steps presented above are implemented again for the new frequency. In this way we always start from a stable configuration, hence limiting the possibility of nonlinear interaction between different modes.

For each forcing frequency, the two limiting amplitude values, identified as described above, are used to define the error bars reported in figure 10. Those error bars must also account for the optical pen's measurement error ($0.1 \mu\text{m}$), as well as the non-uniformity of the output signal. By looking at the measured average, minimum, and maximum amplitude values in the temporal output signal, it is noteworthy that the average value typically deviates from the minimum and maximum by around $10 \mu\text{m}$. Consequently, we incorporate in the error bars this additional $10 \mu\text{m}$ of uncertainty in the value of a . The uncertainty in the frequency of the output signal is not included in the definition of the error bars, as it is extremely small, on the order of 0.001 Hz .

4.4. Instability onset and wave patterns

The experimentally detected threshold at each measured frequency is reported in figure 10 in terms of forcing acceleration f and amplitude a . Once again, the black unstable regions are calculated according to the standard gap-averaged model with $\sigma_{BL} = 12\nu/b^2$, whereas red regions are the unstable tongues computed using the modified damping $\sigma_{BL} = \chi_n\nu/b^2$. Both scenarios include contact line dissipation $\sigma_{CL} = (2M/\rho b)(m/R)\tanh(mh/R)$, with a value of M equal to 0.0485 for ethanol 70%. Although, at first, this value has been simply selected in order to fit well our experimental measurements, it is in perfect agreement with the linear relation linking M to the liquid's surface tension reported in figure 5 of Hamraoui *et al.* (2000) and used by Li *et al.* (2019) (see table 1).

As figure 10 strikingly shows, the present theoretical thresholds match well our experimental measurements. On the contrary, the poor description of the oscillating boundary layer in the classical Darcy model translates into a lack of dissipation. The arbitrary choice of a higher fitting parameter M value, e.g. $M \approx 0.09$ would increase contact line dissipation and compensate for the underestimated Stokes boundary layer one, hence bringing these predictions much closer to experiments; however, such a value would lie well beyond the typical values reported in the literature. Furthermore, the real damping coefficient $\sigma_{BL} = 12\nu/b^2$ given by the Darcy theory does not account for the frequency detuning displayed by experiments. This frequency shift is instead well captured by the imaginary part of the new damping $\sigma_{BL} = \chi_n\nu/b^2$ ($\chi_n = \chi_{n,r} + i\chi_{n,i}$).

Within the experimental frequency range considered, five different standing waves, corresponding to $m = 5, 6, 7, 8$ and 9 , have emerged. The identification of the wavenumber m has been simply performed by visual inspection of the free surface patterns reported in figure 11. Indeed, by looking at two time snapshots separated by a forcing period T , it is possible to count the various wave peaks along the azimuthal direction.

When looking at figure 10, it is worth commenting that on the left sides of the marginal stability boundaries associated with modes $m = 5$ and 6 we still have a little discrepancy between experiments and the model. Particularly, the experimental thresholds are slightly lower than the predicted ones. A possible explanation can be given by noticing that our experimental protocol is agnostic to the possibility of subcritical bifurcations and hysteresis, while such behaviour has been predicted by Douady (1990).

As a last comment, one has to keep in mind that the Hele-Shaw approximation remains good only if the wavelength, $m/2\pi R$ does not become too small, i.e. comparable to the cell's gap, b . In other words, one must check that the ratio $mb/2\pi R$ is of the order of the small

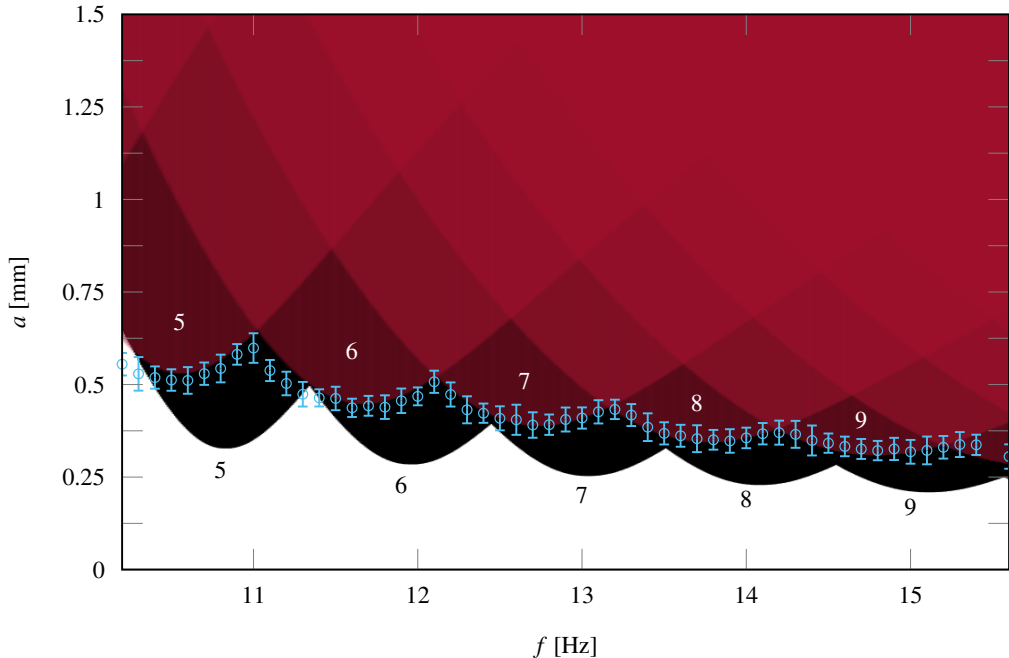


Figure 10: Experiments (empty circles) are compared to the theoretically predicted sub-harmonic Faraday threshold computed via Floquet analysis (2.31) for different fixed azimuthal wavenumber m and according to the standard (black region) and revised (red regions) gap-averaged models. The shaded band around the instability onset indicates the error bar for the threshold amplitudes at each measured driving frequency. The tongues are computed by including contact line dissipation with a value of M equal to 0.0485 as in figures 6(b)-(d) and 8. As explained in §4.3, the vertical error bars indicate the amplitude range between the smallest measured forcing amplitude at which the instability was detected and the largest one at which the surface remains stable and flat. These two limiting values are successively corrected by accounting for the optical pen's measurement error and the non-uniformity of the output signal of the loudspeaker.

separation-of-scale parameter, ϵ . For the largest wavenumber observed in our experiments, $m = 9$, the ratio $mb/2\pi R$ amounts to 0.23, which is not exactly small. Yet, the Hele-Shaw approximation is seen to remain fairly good.

4.5. Contact angle variation and thin film deposition

Before concluding, it is worth commenting on why the use of dynamic contact angle model (2.21) is justifiable and seen to give good estimates of the Faraday thresholds.

Existing lab experiments have revealed that liquid oscillations in Hele-Shaw cells constantly experience an up-and-down driving force with an apparent contact angle θ constantly changing (Jiang *et al.* 2004). Our experiments are consistent with such evidence. In figure 12 we report seven snapshots, (i)-(vii), covering one oscillation period, T , for the container motion. These snapshots illustrate a zoom of the dynamic meniscus profile and show how the macroscopic contact angle changes in time during the second half of the advancing cycle (i)-(v) and the first half of the receding cycle (vi)-(x), hence highlighting the importance of the out-of-plane meniscus curvature variations. Thus, on the basis of our observations, it seems appropriate to introduce in the theory a contact angle model so as to justify this associated additional dissipation, which would be neglected by assuming $M = 0$. The model

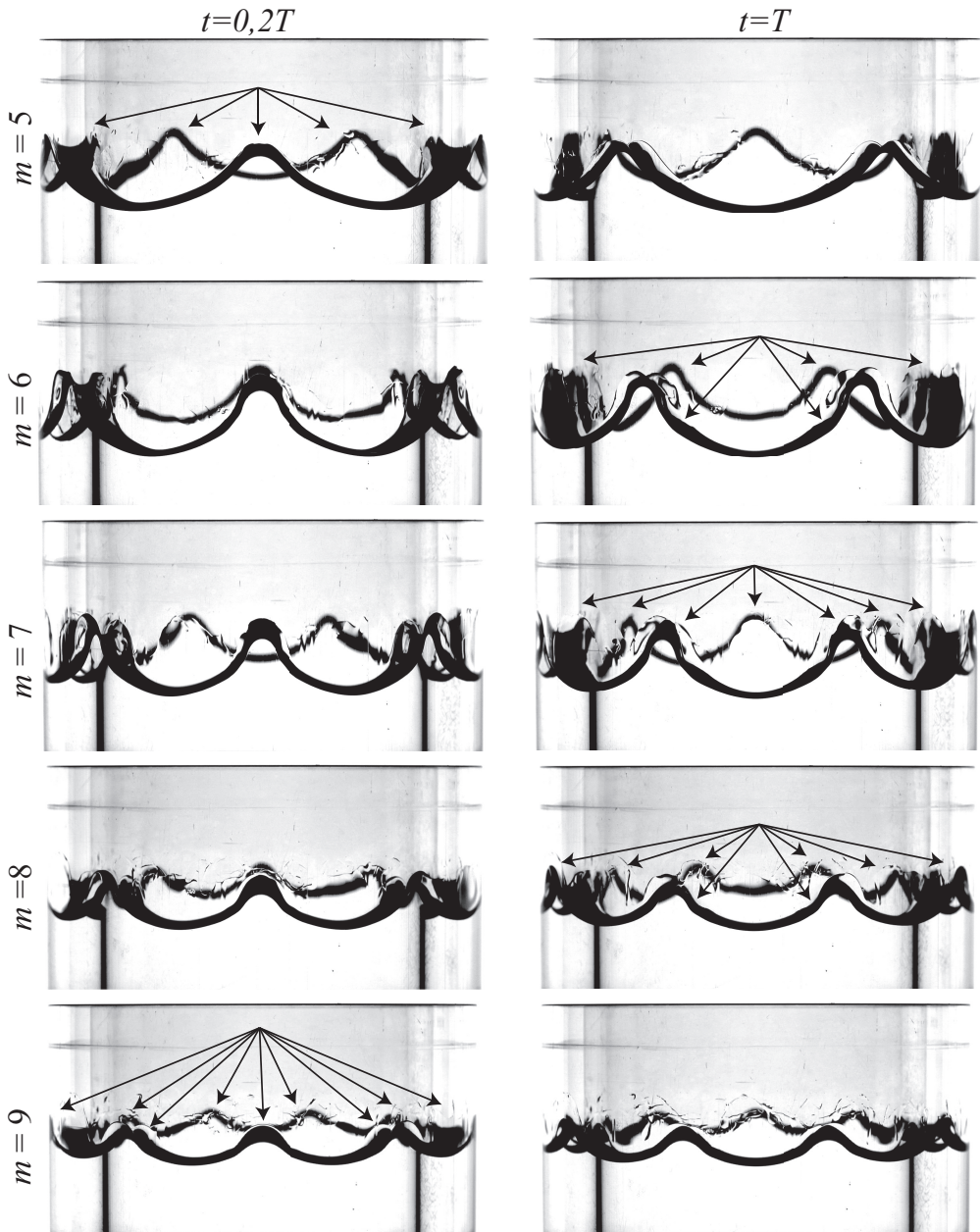


Figure 11: Snapshots of the wave patterns experimentally observed within the sub-harmonic Faraday tongues associated with the azimuthal wavenumbers $m = 5, 6, 7, 8$ and 9 . T is the forcing period, which is approximately half the oscillation period of the wave response. These patterns appear for: ($m = 5$) $1/T = 10.6$ Hz, $a = 0.8$ mm; ($m = 6$) $1/T = 11.6$ Hz, $a = 1.1$ mm; ($m = 7$) $1/T = 12.7$ Hz, $a = 0.9$ mm; ($m = 8$), $1/T = 13.7$ Hz, $a = 0.6$ mm; ($m = 9$) $1/T = 14.8$ Hz, $a = 0.4$ mm. These forcing amplitudes are the maximal achievable at their corresponding frequencies (see figure 8 for the associated operating points). The number of peaks is easily countable by visual inspection of two time snapshots of the oscillating pattern exactred at $t = 0, T$ and $t = T/2$. This provides a simple criterion for the identification of the resonant wavenumber m . See also supplementary movies 1-5 at: [LINK](#).

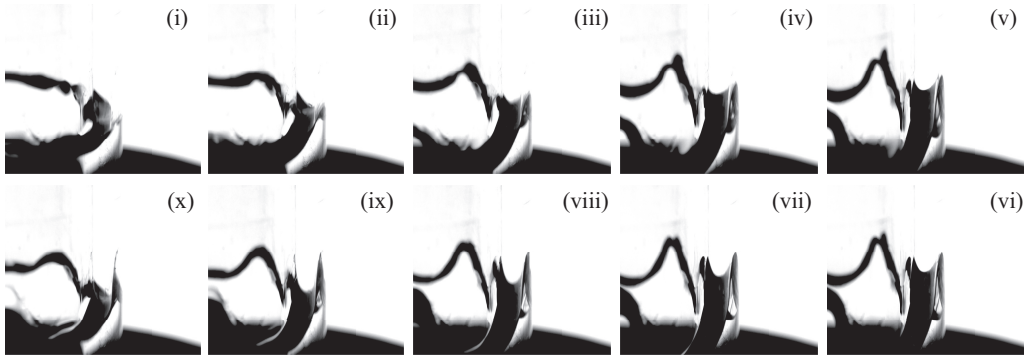


Figure 12: Zoom of the meniscus dynamics recorded at a driving frequency 11.6 Hz and amplitude $a = 1.2$ mm for $m = 6$. Seven snapshots, (i)-(vii), covering one oscillation period, T , for the container motion are illustrated. These snapshots show how the meniscus profile and the macroscopic contact angle change in time during the second half of the advancing cycle and the first half of the receding cycle, hence highlighting the importance of the out-of-plane curvature or capillary effects. . See also supplementary movie 6 at: [LINK](#).

used in this study, and already implemented by Li *et al.* (2019), is very simple; it assumes the cosine of the dynamic contact angle to linearly depend on the contact line speed through the capillary number Ca (Hamraoui *et al.* 2000). Accounting for such a model is shown, both in Li *et al.* (2019) and in this study, to supplement the theoretical predictions by a sufficient extra dissipation suitable to match experimental measurements.

This dissipation eventually reduces to a simple damping coefficient σ_{CL} as it is of linear nature. A unique constant value of the mobility parameter M is sufficient to fit all our experimental measurements at once, suggesting that the meniscus dynamics is not significantly affected by the evolution of the wave in the azimuthal direction, i.e. by the wavenumber, and M can be seen as an intrinsic property of the liquid-substrate interface.

Several studies have discussed the dependence of the system's dissipation on the substrate material (Huh & Scriven 1971; Dussan 1979; Cocciaro *et al.* 1993; Ting & Perlin 1995; Eral *et al.* 2013; Viola *et al.* 2018; Viola & Gallaire 2018; Xia & Steen 2018). These authors, among others, have unveiled and rationalized interesting features such as solid-like friction induced by contact angle hysteresis. This strongly nonlinear contact line behaviour does not seem to be present in our experiments. This can be tentatively explained by looking at figure 13. These snapshots illustrate how the contact line constantly flows over a wetted substrate, due to the presence of a stable thin film deposited and alimanted at each oscillation cycle. This feature has been also recently described by Dollet *et al.* (2020), who showed that the relaxation dynamics of liquid oscillation in a U-shaped tube filled with ethanol, due to the presence of a similar thin film, obey an exponential law that can be well-fitted by introducing a simple linear damping, as done in this work.

5. Conclusions

Previous theoretical analyses for Faraday waves in Hele-Shaw cells have so far relied on the Darcy approximation, which is based on the parabolic flow profile assumption in the narrow direction and that translates into a real-valued damping coefficient $\sigma_{BL} = 12\nu/b^2$, with ν the fluid kinematic viscosity and b the cell's gap-size, that englobes the dissipation originated from the Stokes boundary layers over the two lateral walls. However, Darcy's model is known to be inaccurate whenever inertia is not negligible, e.g. in unsteady flows such as oscillating

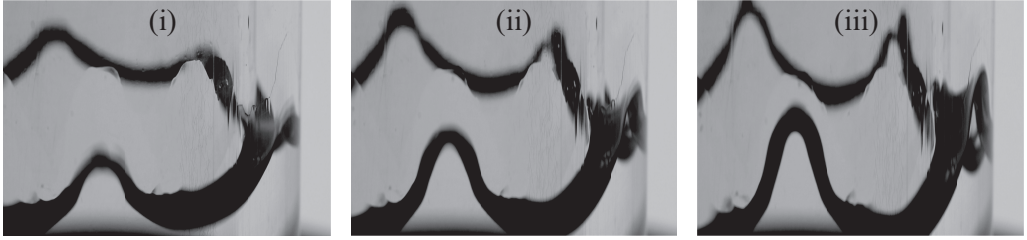


Figure 13: These three snapshots correspond to snapshots (ii), (iii) and (iv) of figure 12 and show, using a different light contrast, how the contact line constantly moves over a wetted substrate due to the presence of a stable thin film deposited and alimeted at each cycle. See also supplementary movies 7 at: [LINK](#).

standing or traveling waves.

In this work, we have proposed a gap-averaged linear model that accounts for inertial effects induced by the unsteady terms in the Navier-Stokes equations, amounting to a pulsatile flow where the fluid's motion reduces to a two-dimensional oscillating, reminiscent of the Womersley flow in cylindrical pipes. When gap-averaging the linearized Navier-Stokes equation, this results in a modified damping coefficient, $\sigma_{BL} = \chi_n \nu / b^2$, with $\chi_n = \chi_{n,r} + i\chi_{n,i}$ complex-valued, which is a function of the ratio between the Stokes boundary layer thickness and the cell's gap-size, and whose value depends on the frequency of the system's response specific to each unstable parametric Faraday tongue.

After having revisited the ideal case of infinitely long rectangular Hele-Shaw cells, we have considered the case of Faraday waves in thin annuli. This annular geometry, owing to the periodicity condition, naturally filters out the additional, although small, dissipation coming from the lateral wall in the elongated direction of finite-size lab-scale Hele-Shaw cells. Hence, a thin annulus offers a prototype configuration that can allow one to better quantify the correction introduced by the present gap-averaged theory when compared to dedicated experiments and to the standard gap-averaged Darcy model.

A series of homemade experiments for the latter configuration has proven that Darcy's model typically underestimates the Faraday threshold, as $\chi_{n,r} > 12$, and overlooks a frequency detuning introduced by $\chi_{n,i} > 0$, which appears essential to correctly predict the location of the Faraday's tongue in the frequency spectrum. The frequency-dependent gap-averaged model here proposed successfully predicts these features and brings the Faraday thresholds estimated theoretically closer to the ones measured.

Furthermore, a close look at the experimentally observed meniscus and contact angle dynamics clearly highlighted the importance of the out-of-plane curvature, whose contribution has been neglected so far in the literature, with the exception of Li *et al.* (2019). This evidence justifies the employment of a dynamical contact angle model to recover the extra contact line dissipation and close the gap with experimental measurements.

A natural extension of this work is to examine the existence of a drift instability at higher forcing amplitudes.

Supplementary Material

Supplementary movies 1-5 show the time evolution of the free surface associated with the snapshots reported in figure 11. Supplementary movies 6 and 7 provide instead better visualizations of the meniscus and the thin film, dynamics, respectively, as illustrated in figures 12 and 13 of this manuscript. Supplementary movies are available at link: [LINK](#).

Funding

We acknowledge the Swiss National Science Foundation under grant 178971.

Declaration of Interests

The authors report no conflict of interest.

Author Contributions

A. B., F. V. and F. G. created the research plan. A.B. formulated analytical and numerical models. A.B. led model solution. A. B. and B. J. designed the experimental setup. B. J. performed all experiments. A.B., B. J., F.V. and F.G. wrote the manuscript.

REFERENCES

- AFKHAMI, S. & RENARDY, Y. 2013 A volume-of-fluid formulation for the study of co-flowing fluids governed by the hele-shaw equations. *Phys. Fluids* **25** (8), 082001.
- BATSON, W., ZOUESHTIAGH, F. & NARAYANAN, R. 2013 The faraday threshold in small cylinders and the sidewall non-ideality. *J. Fluid Mech.* **729** (496-523), 9.
- BENJAMIN, T. B. & URSELL, F. J. 1954 The stability of the plane free surface of a liquid in vertical periodic motion. *Proc. R. Soc. Lond. A* **225** (1163), 505–515.
- BLAKE, T. D. 1993 Dynamic contact angle and wetting kinetics. *Wettability* .
- BLAKE, T. D. 2006 The physics of moving wetting lines. *J. Colloid Interface Sci.* **299** (1), 1–13.
- BONGARZONE, A., VIOLA, F., CAMARRI, S. & GALLAIRE, F. 2022 Subharmonic parametric instability in nearly brimful circular cylinders: a weakly nonlinear analysis. *J. Fluid Mech.* **947**, A24.
- BONGARZONE, A., VIOLA, F. & GALLAIRE, F. 2021 Relaxation of capillary-gravity waves due to contact line nonlinearity: A projection method. *Chaos* **31** (12), 123124.
- CHUOKE, R. L., MEURS, P. VAN & VAN DER POEL, C. 1959 The instability of slow, immiscible, viscous liquid-liquid displacements in permeable media. *Trans. Am. Inst.* **216** (01), 188–194.
- COCCIARO, B., FAETTI, S. & FESTA, C. 1993 Experimental investigation of capillarity effects on surface gravity waves: non-wetting boundary conditions. *J. Fluid Mech.* **246**, 43–66.
- DOLLET, B., LORENCEAU, É. & GALLAIRE, F. 2020 Transition from exponentially damped to finite-time arrest liquid oscillations induced by contact line hysteresis. *Phys. Rev. Lett.* **124** (10), 104502.
- DOUADY, S. 1990 Experimental study of the Faraday instability. *J. Fluid Mech.* **221**, 383–409.
- DOUADY, S., FAUVE, S. & THUAL, O. 1989 Oscillatory phase modulation of parametrically forced surface waves. *EPL* **10** (4), 309.
- DUSSAN, E. B. 1979 On the spreading of liquids on solid surfaces: static and dynamic contact lines. *Ann. Rev. Fluid Mech.* **11** (1), 371–400.
- ERAL, H. B., MANNETJE, J. C. M. 'T & OH, J. M. 2013 Contact angle hysteresis: a review of fundamentals and applications. *Colloid Polym. Sci.* **291** (2), 247–260.
- FARADAY, M. 1831 *Phil. Trans.* .
- FAUVE, S., DOUADY, S. & THUAL, O. 1991 Drift instabilities of cellular patterns. *J. Phys. II* **1** (3), 311–322.
- GONDRET, P. & RABAUD, M. 1997 Shear instability of two-fluid parallel flow in a hele-shaw cell. *Phys. Fluids* **9** (11), 3267–3274.
- HAMRAOUI, A., THURESSON, K., NYLANDER, T. & YAMINSKY, V. 2000 Can a dynamic contact angle be understood in terms of a friction coefficient? *J. Colloid Interface Sci.* **226** (2), 199–204.
- HOCKING, L. M. 1987 The damping of capillary-gravity waves at a rigid boundary. *J. Fluid Mech.* **179**, 253–266.
- HUH, C. & SCRIVEN, L. E. 1971 Hydrodynamic model of steady movement of a solid/liquid/fluid contact line. *J. Colloid. Interf. Sci.* **35** (1), 85–101.
- JIANG, L., PERLIN, M. & SCHULTZ, W. W. 2004 Contact-line dynamics and damping for oscillating free surface flows. *Phys. Fluids* **16** (3), 748–758.
- JOHANSSON, P. & HESS, B. 2018 Molecular origin of contact line friction in dynamic wetting. *Phys. Rev. Fluids* **3** (7), 074201.
- KALOGIROU, A., MOULOPOULOU, E. E. & BOKHOVE, O. 2016 Variational finite element methods for waves in a hele-shaw tank. *App. Math. Model.* **40** (17-18), 7493–7503.

- KUMAR, K. & TUCKERMAN, L. S. 1994 Parametric instability of the interface between two fluids. *J. Fluid Mech.* **279**, 49–68.
- LAMB, H. 1993 *Hydrodynamics*. Cambridge University Press.
- LI, J., LI, X., HEN, K., XIE, B. & LIAO, S. 2018a Faraday waves in a hele-shaw cell. *Physics of Fluids* **30** (4), 042106.
- LI, J., LI, X. & LIAO, S. 2019 Stability and hysteresis of faraday waves in hele-shaw cells. *J. Fluid Mech.* **871**, 694–716.
- LI, X., LI, J., LIAO, S. & CHEN, C. 2018b Effect of depth on the properties of two coupled faraday waves in a hele-shaw cell. *Phys. Fluids* **30** (10), 102103.
- LI, X., LI, X. & LIAO, S. 2016 Pattern transition of two-dimensional faraday waves at an extremely shallow depth. *Sci. China Phys. Mech.* **59**, 1–3.
- LI, X., XU, D. & LIAO, S. 2014 Observations of highly localized oscillons with multiple crests and troughs. *Phys. Rev. E* **90** (3), 031001.
- LI, X., YU, Z. & LIAO, S. 2015 Observation of two-dimensional faraday waves in extremely shallow depth. *Phys. Rev. E* **92** (3), 033014.
- LUCHINI, P. & CHARRU, F. 2010 Consistent section-averaged equations of quasi-one-dimensional laminar flow. *J. Fluid Mech.* **656**, 337–341.
- MCLEAN, J. W. & SAFFMAN, P. G. 1981 The effect of surface tension on the shape of fingers in a hele-shaw cell. *J. Fluid Mech.* **102**, 455–469.
- MÜLLER, H. W., WITTMER, H., WAGNER, C., ALBERS, J. & KNORR, K. 1997 Analytic stability theory for faraday waves and the observation of the harmonic surface response. *Phys. Rev. Lett.* **78** (12), 2357.
- NAYFEH, A. H. 2008 *Perturbation Methods*. Wiley.
- O. V. VOINOV, OV 1976 Hydrodynamics of wetting. *Fluid Dyn.* **11** (5), 714–721.
- PARK, C.-W. & HOMS, G. M. 1984 Two-phase displacement in hele shaw cells: theory. *J. Fluid Mech.* **139**, 291–308.
- PÉRINET, N., FALCÓN, C., CHERGUI, J., JURIC, D. & SHIN, S. 2016 Hysteretic faraday waves. *Phys. Rev. E* **93** (6), 063114.
- PLOURABOUÉ, F. & HINCH, E. J. 2002 Kelvin–helmholtz instability in a hele-shaw cell. *Phys. Fluids* **14** (3), 922–929.
- POPINET, S. 2003 Gerris: a tree-based adaptive solver for the incompressible euler equations in complex geometries. *J. Comp. Physics* **190** (2), 572–600.
- POPINET, S. 2009 An accurate adaptive solver for surface-tension-driven interfacial flows. *J. Comp. Physics* **228** (16), 5838–5866.
- RAJCHENBACH, J. & CLAMOND, D. 2015 Faraday waves: their dispersion relation, nature of bifurcation and wavenumber selection revisited. *J. Fluid Mech.* **777**, R2.
- RAJCHENBACH, J., LEROUX, A. & CLAMOND, D. 2011 New standing solitary waves in water. *Phys. Rev. Lett.* **107** (2), 024502.
- RUYER-QUIL, C. 2001 Inertial corrections to the darcy law in a hele–shaw cell. *Comptes Rendus de l'Académie des Sciences-Series IIB-Mechanics* **329** (5), 337–342.
- SAFFMAN, P. G. & TAYLOR, G. I. 1958 The penetration of a fluid into a porous medium or hele-shaw cell containing a more viscous liquid. *Proc. R. Soc. A: Math. Phys. Eng. Sci.* **245** (1242), 312–329.
- SAN, OMER & STAPLES, ANNE E 2012 An improved model for reduced-order physiological fluid flows. *J. Mech. Med. Biol.* **12** (03), 1250052.
- TING, C.-L. & PERLIN, M. 1995 Boundary conditions in the vicinity of the contact line at a vertically oscillating upright plate: an experimental investigation. *J. Fluid Mech.* **295**, 263–300.
- UBAL, S., GIAVEDONI, M. D. & SAITA, F. A. 2003 A numerical analysis of the influence of the liquid depth on two-dimensional faraday waves. *Phys. Fluids* **15** (10), 3099–3113.
- VIOLA, F., BRUN, P.-T. & GALLAIRE, F. 2018 Capillary hysteresis in sloshing dynamics: a weakly nonlinear analysis. *J. Fluid Mech.* **837**, 788–818.
- VIOLA, F. & GALLAIRE, F. 2018 Theoretical framework to analyze the combined effect of surface tension and viscosity on the damping rate of sloshing waves. *Phys. Rev. Fluids* **3** (9), 094801.
- VIOLA, F., GALLAIRE, F. & DOLLET, B. 2017 Sloshing in a hele-shaw cell: experiments and theory. *J. Fluid Mech.* **831**.
- WOMERSLEY, J. R. 1955 Method for the calculation of velocity, rate of flow and viscous drag in arteries when the pressure gradient is known. *Physiol. J.* **127** (3), 553.
- XIA, Y. & STEEN, P. H. 2018 Moving contact-line mobility measured. *J. Fluid Mech.* **841**, 767–783.